to compressive effects, the density perturbation at the end wall also increases with time, but at a slower rate than the perturbation at the shock wave. The unsteady reflection process thus creates a negative gradient in density toward the end wall.

An examination of Eq. (11) shows that the temperature perturbation just behind the reflected shock front is negative and becomes more negative with time, whereas the perturbation at the end wall is positive and increases with time. In fact, there is a growing region of gas near the end wall, of width $[(\gamma - 1)K/I]\hat{x}$, wherein the temperature perturbation is positive and increases steadily with time.

This unexpected result for the temperature can be explained as follows. Implicit in the conservation equations for steady, one-dimensional flow of an ideal gas is the requirement that the flow in region 2 lose thermal energy in order for the density to increase. This energy loss is responsible for the negative temperature perturbation immediately behind the reflected shock wave. Whatever the mechanism for energy extraction from region 2, the momentum of this gas is increased, and this increase in momentum manifests itself as a pressure rise in region 5. The net effect is that compressive work is continually being done on the gas in region 5, thus adding thermal energy along each particle path. Furthermore, the rate of energy addition is the same along all particle paths since the pressure rises uniformly. The energy of a particular gas element at any given time thus depends on the initial thermal energy of the element upon entering region 5 and the length of time spent in region 5.

Some of the results obtained here for an ideal gas are of use in understanding the shock-reflection process when density gradients are present in nonideal gases. Although the numerical results may differ, many of the important physical concepts are retained. For example, one must conclude that radiative cooling behind an incident shock wave, a nonadiabatic effect which would increase the density in region 2, should also cause an entropy layer. If radiative cooling occurs in region 2, one may thus expect a trend toward higher temperatures near the end wall and lower temperatures near the reflected shock wave. In a real case, of course, when energy is being lost by means of radiation from region 2, region 5 may also be losing energy, and this fact would have to be included in any meaningful calculation.

Since vibrational and chemical relaxation cause a density increase behind the incident shock wave, the present model also accounts for the principal features of reflected-shock flowfields in relaxing gases. This connection is possible since relaxation effects in region 5 may be considered part of the reflected-shock structure (owing to the comparatively fast relaxation at the higher temperature and density of region 5). One would thus expect entropy layers with positive temperature perturbations and negative density perturbations near the end wall.[1,2]

For cases involving relaxation, only a limited density change occurs in region 2 so the resulting perturbations in region 5 eventually approach a steady-state distribution. This limiting behavior is clearly exhibited in Fig. 2, which presents a measurement of the pressure on a shock-tube end wall during the reflection process in vibrationally relaxing nitrogen.[4] The sharp rise in pressure corresponds to the arrival of the shock wave at the end wall while the subsequent gradual rise in pressure represents the perturbation caused by the relaxation in region 2.

After steady-state conditions are reached, the reflected shock moves away from the end wall at a steady speed, leaving behind a growing region of gas with a uniform equilibrium state and a stationary entropy layer adjacent to the end wall. The thickness of such an entropy layer scales directly with the length of the incident-shock relaxation zone, and is essentially that relaxation length compressed by the density ratio across the reflected shock wave.

References

[1] Johannesen, N. H., Bird, G. A., and Zienkiewicz, H. K., "Theoretical and Experimental Investigations of the Reflection of Normal Shock Waves with Vibrational Relaxation," *Journal of Fluid Mechanics*, Vol. 30, Pt. 1, 1967, pp. 51–64.

[2] Presley, L. L. and Hanson, R. K., "Numerical Solutions of Reflected Shock-Wave Flowfields with Nonequilibrium Chemical Reactions," *AIAA Journal*, Vol. 7, No. 12, Dec. 1969, pp. 2267–2273.

[3] Rudinger, G., "Effect of Boundary-Layer Growth in a Shock Tube on Shock Reflection From a Closed End," *The Physics of Fluids*, Vol. 4, 1961, pp. 1463–1473.

[4] Hanson, R. K., "An Experimental and Analytical Investigation of Shock-Wave Reflection in a Relaxing Gas," SUDAAR 345, May 1968, Stanford Univ., Stanford, Calif.

Computation of Current Sheet Speeds in Plasma Accelerators

R. J. WOLF*

AND

F. Y. SORRELL†

University of Colorado, Boulder, Colo.

AND

Y. NAKAGAWA‡

National Center for Atmospheric Research, Boulder, Colo.

WHEN it is desired to produce very high current sheet speeds in plasma accelerators, it is usually necessary to use very large currents. To obtain these currents the external circuit inductance is usually reduced as much as practical and generally results in a condition where the accelerator inductance and its time change govern the drive current, rather than the external circuit. In order to investigate this we have used the snowplow[1] model to give the current sheet position and a circuit equation that assumes a fixed external circuit inductance in series with a time dependent inductance (the accelerator). No circuit resistance is included. This technique has been used previously[2] and thus the purpose of this Note is not to introduce the computation technique, but to present some new and useful results.

We wish to use this technique to compute the speed of the current sheet in a coaxial accelerator, and in this device the force on the current sheet varies with the radius squared. Thus, one must either apply the snowplow model at some mean radius, or, as was done here, apply the equations at several radii. To do this, a separate momentum balance is made at each of 5 equally spaced radii and the position of the current layer is computed at each radius. This will give a parabolic shaped current sheet which should approximate that found experimentally by Keck[3] for this geometry. When this is done the snowplow equation for the distance of the current layer from the insulator of the accelerator, x_i, at the radius r_i is

$$d/dt[\rho_1 x_i(dx_i/dt)] = \mu_0 I^2/8\pi^2 r_i^2 \quad (1)$$

Received November 10, 1969. This work was supported in part by the National Center for Atmospheric Research and in part by the National Science Foundation grant GK-1202.

* Graduate student, Department of Aerospace Engineering Sciences.

† Assistant Professor, Department of Aerospace Engineering Sciences; now Assistant Professor, Department of Engineering Mechanics, North Carolina State University, Raleigh, N.C.

‡ Physicist, high altitude observatory.

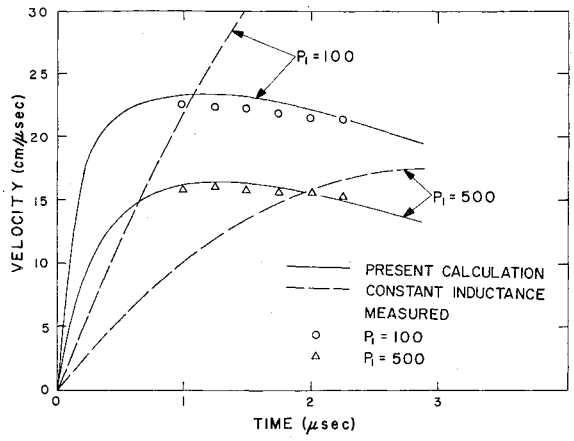

Fig. 1 Measured current sheath speeds in the NCAR accelerator compared with those calculated from the present model and the constant inductance model.

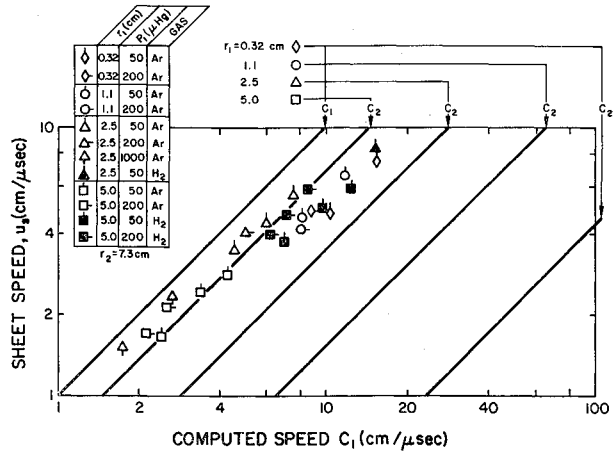

Fig. 3 Speeds in a coaxial accelerator as measured by Keck and the speeds C_1 and C_2 computed here.

where I is the accelerator current, μ_0 is the magnetic permeability of free space, and ρ_1 is the initial mass density. This equation is coupled to the equation for the current, I, which is

$$(L_0 + L)\ddot{I} + 2\dot{L}\dot{I} + (1/C + \ddot{L})I = 0 \qquad (2)$$

where L_0 is the fixed external circuit inductance, L is the time dependent accelerator inductance, and C is the energy storage capacitance; by the equation for the time dependent inductance,

$$L(t) = \frac{\mu_0}{2\pi} \sum_i \ln\left(\frac{r_i + 1}{r_i}\right)\left[\frac{x_{i+1} + x_i}{2}\right] \qquad (3)$$

Equations (1, 2, and 3) were solved numerically to give the current sheet speed as a function of time. The computed speeds at the inner electrode of a coaxial accelerator with an inner radius of 2.375 cm, an outer radius of 4.25 cm operating in hydrogen with circuit inductance L_0 of 20 nanohenries and energy storage capacitance of 85 μf are shown in Fig. 1. This is the accelerator currently being used at NCAR, and the experimental data presented in the same figure are speeds at the inner electrode as determined by streak camera photographs. The speed for a constant inductance of 30 nanohenries is also shown for comparison. Note that both the measured and computed speeds are nearly constant while the fixed inductance solution predicts a much greater variation in time. This is because the time dependent inductance modifies the current waveform in such a way as to decrease the speed and make it relatively constant. Also, the increase in speed with decreasing pressure or increasing voltage is much less than that given by the constant inductance model. The constant inductance solution predicts a current sheet speed that is proportional to the initial capacitor voltage, V_0, and inversely proportional to $\rho_1^{1/2}$. However, a curve fit to the preceding calculations shows the speed is proportional to $V_0^{1/2}\rho_1^{-1/4}$, for speeds between 18 and 40 cm/μsec.

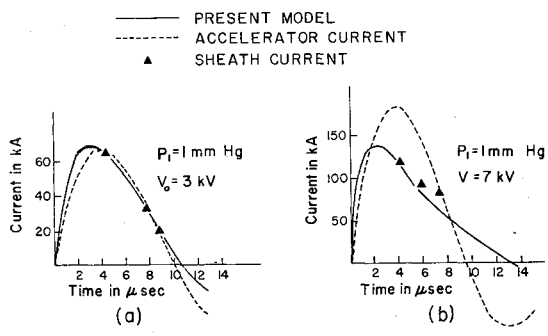

Fig. 2 Accelerator and sheath current measured by Dattner & Eninger and the accelerator current computed by the present model.

We have confirmed that the decrease in speed is due to a reduction in drive current by a comparison of the computed and measured current in the accelerator. The constant inductance current was also verified by shorting the accelerator electrodes. In addition, the modification of the current waveform to give nearly constant speeds was also observed.

It is quite interesting to compare our numerical results with existing experimental data. In the experiments discussed now the measured acclerator current was higher than the current we compute for that particular experiment. Usually, it is nearly the current predicted by a constant inductance model. It is not clear how such large currents are obtained; possibly a substantial part of the current does not move down the accelerator, but remains at the insulator. This would of course reduce the speed of that current that did propagate down the accelerator. In most of these cases we also find close agreement between the speeds we compute and those measured experimentally. Speculation as to why the measured current exceeds the value we compute and the measured sheath speeds or sheath currents agree with our calculations is carefully avoided; however, several illustrations are given.

Dattner and Eninger[4] have determined the current within the current sheath by measuring the change in magnetic field across the sheath. They also measured the total accelerator current. Their results are shown in Fig. 2 with our computation for the accelerator current. Please note the agreement between all three methods when the effect of the time varying inductance is expected to be small (3kV) and agreement between our computation of the accelerator current and their measurements of the current within the sheath when the effect of the time varying inductance is not negligible.

Keck[5] has carried out a very thorough investigation of the dependence of current layer speed on experimental parameters in a coaxial accelerator. Generally, he observed the current layer speed to be less than that computed from the measured current. Using the present model, we have computed the speed C_1 at the inner electrode and C_2 at the outer electrode for Keck's experimental conditions. These results are shown in Fig. 3 using the same format as Keck (Fig. 7 of Ref. 5). In this figure the only difference from that given in Ref. 5 is that the computed speeds are calculated from our model, rather than the measured accelerator current. Again, the agreement between our calculated and Keck's measured speeds are usually good. The present model has used a lumped capacitor and inductor in the external circuit and

Keck's experiments were with a transmission line circuit. However, when the current becomes limited by the changing accelerator inductance rather than the external circuit, the eternal circuit has little effect on the accelerator current. Thus, the present computations are expected to accurately predict the speeds, particularly at speeds above 8 cm/μsec.

Patrick[6] has reported speeds in a coaxial accelerator from 20 to 40 cm/μsec. We have attempted to duplicate his experimental conditions, but the present models give speeds of 18–22 cm/μsec.

References

[1] Greifinger, C. and Cole, J. D., "Similarity Solution for Cylindrical Magnetohydrodynamic Blast Waves," *The Physics of Fluids*, Vol. 5, No. 12, Dec. 1962, pp. 1597–1607.

[2] Hart, P. J., "Plasma Acceleration with Coaxial Electrodes," *The Physics of Fluids*, Vol. 5, No. 1, Jan. 1962, pp. 38–47.

[3] Keck, J. C., Fishman, F., and Petschek, H., "Current Distribution in a Magnetic Annular Shock Tube," *The Physics of Fluids*, Vol. 5, No. 5, May 1962, pp. 630–632.

[4] Dattner, A. and Eninger, J., "Studies of a Coaxial Plasma Gun," *The Physics of Fluids Supplement*, Vol. 7, No. 11, Nov. 1964, pp. S41–S43.

[5] Keck, J., "Current Speed in a Magnetic Annular Shock Tube," *The Physics of Fluids Supplement*, Vol. 7, No. 11, Nov. 1964, pp. S16–S27.

[6] Patrick, R. M., "High Speed Shock Waves in a Magnetic Annular Shock Tube," *The Physics of Fluids*, Vol. 2, No. 6, June 1959, pp. 589–598.

A Parallel between Keplerian Integrals and Integrals of the Adjoint Equations

I. F. Burns*

Northrop-Huntsville, Huntsville, Ala.

A CLASSICAL development of the Keplerian vector constants, angular momentum and the perifocus vector (Hamilton's integral), is presented. A similar procedure is applied to the combined motion and adjoint equations to derive two additional vector constants, analogous in algebraic form to the Keplerian integrals, one which is apparently new. A full set of six independent integrals for the adjoint variables is obtained by adjoining to the two vector constants a known integral explicitly dependent upon time.

I. Introduction

There has been recent interest[1-2] in finding integrals of the system

$$\ddot{\bar{X}} = (F/m\Lambda)\bar{\lambda} - (\mu/R^3)\bar{X} \tag{1}$$

$$\ddot{\bar{\lambda}} = -(\mu/R^3)\{\bar{\lambda} - [3/R^2](\bar{\lambda}\cdot\bar{X})\bar{X}\} \tag{2}$$

where $\bar{X}$ and $\dot{\bar{X}}$ represent position and velocity vectors relative to an earth centered, orthogonal, nonrotating coordinate system with gravitational constant μ. The vector $\bar{\lambda}$ is adjoint to $\dot{\bar{X}}$ and the magnitudes of $\bar{\lambda}$, $\bar{X}$, and $\dot{\bar{X}}$ are denoted Λ, R, and V, respectively. Equations (1) and (2) govern the optimum (maximum payload) trajectory of a powered vehicle in an inverse square gravitational field. The vehicle's mass, m, is assumed to vary linearly with time on finite thrust arcs and to be constant on coast arcs. When the thrust magnitude, F, is allowed to become large or even unbounded the resulting optimal trajectories characteristically become some sequence of short thrust arcs ($F = F_{MAX} > 0$) and relatively long Keplerian coast arcs ($F = 0$). As a first step in finding integrals for Eqs. (1) and (2) one might consider only the coast arcs. In the special case where the thrust magnitude is unbounded and the thrust arcs are infinitesimal (impulses), the integrals for coast arcs may easily be extended to account for the impulses.

Received November 20, 1969. This work was sponsored by NASA Marshall Space Flight Center, Huntsville, Ala. under contract NAS8-20082. The author wishes to express his gratitude to R. Silber for many motivating discussions and his encouragement for publishing this Note.

* Senior Engineer.

II. Derivation of the Integrals

Unpowered flight ($F = 0$) is considered first. Conservation of angular momentum is shown by crossing Eq. (1) from the left by $\bar{X}$ and observing that

$$\bar{X} \times \ddot{\bar{X}} = (d/dt)(\bar{X} \times \dot{\bar{X}}) = (d/dt)(\bar{L}) = 0 \tag{3}$$

If one treats the combined Eqs. (1) and (2) similarly with $\bar{X}$ and $\bar{\lambda}$, then $\bar{\lambda} \times \ddot{\bar{X}} = -(\mu/R^3)\bar{X} \times \bar{\lambda}$ and $\bar{X} \times \ddot{\bar{\lambda}} = -(\mu/R^3)\bar{X} \times \bar{\lambda}$. Adding these equations yields

$$\bar{\lambda} \times \ddot{\bar{X}} + \bar{X} \times \ddot{\bar{\lambda}} = (d/dt)(\bar{\lambda} \times \dot{\bar{X}} + \bar{X} \times \dot{\bar{\lambda}}) = (d/dt)(\bar{L}^*) = 0 \tag{4}$$

Note that Eq. (4) holds also for powered arcs.

The similarity of the respective derivations of $\bar{L}$ and $\bar{L}^*$ and the algebraic forms motivates one to seek a corresponding relation to Hamilton's integral, $\bar{M}$. Continuing then, consider

$$(d/dt)(\dot{\bar{X}} \times \bar{L}) = -(\mu/R^3)\bar{X} \times \bar{L} = -(\mu/R^3)[(\bar{X}\cdot\dot{\bar{X}})\bar{X} - R^2\dot{\bar{X}}] \tag{5}$$

But

$$(d/dt)[(\mu/R)\bar{X}] = -(\mu/R^3)[(\bar{X}\cdot\dot{\bar{X}})\bar{X} - R^2\dot{\bar{X}}] \tag{6}$$

whence

$$(d/dt)[\dot{\bar{X}} \times \bar{L} - (\mu/R)\bar{X}] = (d/dt)(\bar{M}) = 0 \tag{7}$$

By analogy then

$$(d/dt)(\dot{\bar{X}} \times \bar{L}^* + \dot{\bar{\lambda}} \times \bar{L}) = -(\mu/R^3) \times [\dot{\bar{\lambda}}\cdot\bar{X} + \bar{\lambda}\cdot\dot{\bar{X}} - (3/R^2)(\bar{\lambda}\cdot\bar{X})(\bar{X}\cdot\dot{\bar{X}})]\bar{X} - (\mu/R^3)(\bar{\lambda}\cdot\bar{X})\bar{X} - (\mu/R^3)(\bar{X}\cdot\dot{\bar{X}})\bar{\lambda} + (\mu/R)\dot{\bar{\lambda}} \tag{8}$$

The right-hand side of Eq. (8) is $(d/dt)\ [\mu/R\bar{\lambda} - (\mu/R^3)(\bar{\lambda}\cdot\bar{X})\bar{X}]$ from which one obtains

$$(d/dt)[\dot{\bar{X}} \times \bar{L}^* + \dot{\bar{\lambda}} \times \bar{L} - (\mu/R)\bar{\lambda} + (\mu/R^3)(\bar{\lambda}\cdot\bar{X})\bar{X}] = (d/dt)(\bar{M}^*) = 0 \tag{9}$$

The constant $\bar{M}^*$ has nearly the same interesting relation to $\bar{M}$ as does $\bar{L}^*$ to $\bar{L}$.

In the derivation of $\bar{M}^*$ with nonzero thrust terms included, Eq. (9) becomes

$$(d/dt)(\bar{M}^*) = (F/m\Lambda)\{\dot{\bar{\lambda}} \times (\bar{X} \times \bar{\lambda}) + \bar{\lambda} \times \bar{L}^*\} \tag{10}$$

As in Ref. 2, Eq. (10) may be integrated over infinitesimal thrust arcs. Thus at any time t, greater than the initial time t_o, in which p such thrust arcs have been traversed, each at times t_i $i = 1, \ldots, p$, Eq. (10) may be integrated

$$\int_{t_o}^{t} \frac{d}{dt}(\bar{M}^*) = \sum_{i=1}^{p} \int_{t_i^-}^{t_i^+} \frac{F}{m\Lambda}\{\dot{\bar{\lambda}} \times (\bar{X} \times \bar{\lambda}) + \bar{\lambda} \times \bar{L}^*\}$$

then

$$\bar{M}^* - \bar{M}_o^* = \sum_{i=1}^{p} \frac{1}{\Lambda_i}\{\dot{\bar{\lambda}} \times (\bar{X} \times \bar{\lambda}) + \bar{\lambda} \times \bar{L}^*\}_i \int_{t_i^-}^{t_i^+} \frac{F}{m}\,dt \tag{11}$$